INTERNATIONAL JOURNAL OF HYDROGEN ENERGY 44 (2019) 23396–23405

Available online at www.sciencedirect.com

ScienceDirect

journal homepage: www.elsevier.com/locate/he

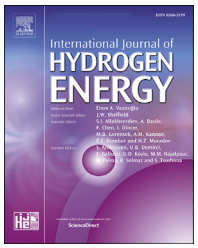

Effect of compression on pore size distribution and porosity of PEM fuel cell catalyst layers

Ali Malekian [a], *Sina Salari* [a], *Juergen Stumper* [b], *Ned Djilali* [c], *Majid Bahrami* [a,*]

[a] *Laboratory for Alternative Energy Conversion (LAEC), School of Mechatronic Systems Engineering, Simon Fraser University, Surrey, BC V3T 0A3, Canada*

[b] *Automotive Fuel Cell Cooperation, 9000 Glenlyon Parkway, Burnaby, BC, V5J 5J8, Canada*

[c] *Department of Mechanical Engineering and Institute for Integrated Energy Systems, University of Victoria, Victoria V8P 5C2, BC, Canada*

HIGHLIGHTS

- Porosity of CL decreases non-linearly with compressive load (11–17%).
- Reduction of larger pores under compression is more significant than smaller ones.
- CL pore diameter decreases between 20 and 50% under 5 MPa pressure.
- PSD has a shift toward smaller pores due to a significant decrease in larger pores.
- Volume percentage of smaller pores increases under compression.

ARTICLE INFO

Article history:
Received 19 February 2019
Received in revised form
2 July 2019
Accepted 5 July 2019
Available online 31 July 2019

Keywords:
Catalyst layer
Compression
Porosity
Pore size distribution
Mechanical properties
Modeling

ABSTRACT

In this study, effects of compression (up to 5 MPa) on pore size distribution (PSD) and porosity of catalyst layers (CL) are investigated using a developed model for deformation of CL under compression. The model is based on effective medium theory and uses a representative geometry (unit cell) to simplify the complex and random porous structure of CL. In this model, different sizes are found for unit cells which are based on CL PSD measurement; this means that unit cell size has distribution since PSD is used as an input to the model. The model has been validated with experimental data in our previous publications. Effect of compression on four different CL samples is studied using the developed model and change of pore diameter is found as function of compression. The change of pore size is different for each sample and dependents on CL initial porosity, PSD, and ink properties. PSD and porosity, which are the indications of microstructure of CL, are found after compression up to 5 MPa. Larger pores show the most change, which causes the void volume percentage of smaller pores to increase, even though the number of pores remain the same. It is also found that the diameter of secondary pores can be decreased by up to 50% depending on CL microstructure, which is significant.

* *Corresponding author.*
E-mail addresses: amalekia@sfu.ca (A. Malekian), mbahrami@sfu.ca (M. Bahrami).

https://doi.org/10.1016/j.ijhydene.2019.07.036

Introduction

The Membrane Electrode Assembly (MEA) in a PEM fuel cell undergoes numerous temperature, humidity, and compression cycles in the manufacturing and operation processes. This cyclic change affects the microstructure of the layers inside fuel cell, which leads to changes in properties of the layers. Hence, lifetime, efficiency, and performance of PEM fuel cells change significantly with these cyclic loadings [1–3]. Also, the heat and water generated within the MEA induces hygrothermal stresses in layers, which change the MEA properties significantly. Hence, it is important to model and measure the mechanical properties of the MEA layers under compression.

Among different layers in MEA (membrane, microporous layer, catalyst layers (CL), and gas diffusion layers (GDL)), CL is the core of PEM fuel cell. This is because of the continuous electrochemical reactions that occur in the CL, which produce water and heat. Hence, in-depth understanding of mechanical, thermal, electrical, and transport properties of CL is crucial to predict the performance of PEM fuel cells and to increase their efficiency and reliability. Mechanical properties of CL (e.g. Young's modulus) plays an important role since other properties, such as thermal conductivity and gass diffusivity, are dependent on compressive load and how the material deforms under compression. Moreover, by applying compressive load on CL, its thickness decreases and its microstructure (e.g. pore sizes, porosity, and pore size distribution) changes notably. And since the microstructure of CL is a factor in predicting and modeling thermal and transport properties of CL, understanding the change in microstructure as a function of compression becomes important. The focus of this paper is the effect of compression on CL pore size distribution and porosity.

Pore size distribution (PSD) along with porosity are the most important microstructural properties of CL since oxygen needs to diffuse to cathode side for the reaction to happen and also the generated water needs to be removed from CL. As shown in our previous publications [4–6], PSD is the key to model diffusivity and mechanical deformation, so PSD is needed to predict properties of CL. Moreover, compressive load decreases porosity and changes PSD, which makes it important to understand how the PSD changes under compression. By knowing the PSD under compression, one can predict other properties such as gas diffusivity under compression.

There are several experimental studies on CL mechanical properties available in the literature. Among these, publications on mechanical properties of CL by Fuel Cell System Development Div. at Toyota in Japan are notable [2,7–9]. Papers by Sassin et al. [10] and Shen [11] are also experimental studies on mechanical properties of CL. However, only a few studies are available on modeling CL mechanical properties [6,12,13].

Sassin et al. [10] reported the influence of compressive load on MEAs and found that although the pore structure of the microporous layer (MPL) and gas diffusion media (GDM) were significantly altered at compressive stresses greater than about 0.9 MPa, the CL structure remained unaltered up to 1.4 MPa, the maximum compressive stress investigated. Shen [11] also measured Young's modulus of CL using a nano-indentation technique. They found that the Young's modulus increased as the indentation in CL increased which was consistent with the results that we published recently [5].

In order to determine the effect of compression on PSD and porosity, mechanical behaviour or pressure-strain curve of CL is needed. In another study by our group [5,6], deformation of CL is found experimentally and modeled analytically. The model was developed to predict the mechanical behaviour of CL under compression using a representative medium theory. Deformation of the ionomer that covers the agglomerates was found to be the dominant deformation mode in CL under compression. The developed model was validated using experimental results that were published in Ref. [5]. Also, the same simplified geometry was used to model gas diffusivity and thermal conductivity of CL and they are validated using experimental results; please see other publication from our group [4,14,15].

The present study provides a platform to predict PSD under compression that is key for estimating other properties of CL under compression. In this study, an overview of our representative geometry and compression model is described. Also, the effect of compression on primary pores and secondary pores is found, then variation in pores diameter for four CL samples is calculated using the model. Based on the change in pores diameter, new PSD after compression is obtained by the model. The results of the model are compared with an experimental study available in the literature. Effect of compression on porosity, which is another indication of microstructure, is also found using the model and validated by experiments.

Deformation of CL under compression

Microstructure and geometrical model of CL

Catalyst layer is a random porous layer consist of carbon particles, ionomer, and Pt particles that are supported on the carbon particles (Fig. 1). Agglomerate is a cluster of carbon particles that is covered with ionomer and they are connected in the entire medium. Generally, there are two types of pores in CL: i) primary pores (less than ~20 nm), ii) secondary pores (30–150 nm). Primary pores are between carbon particles

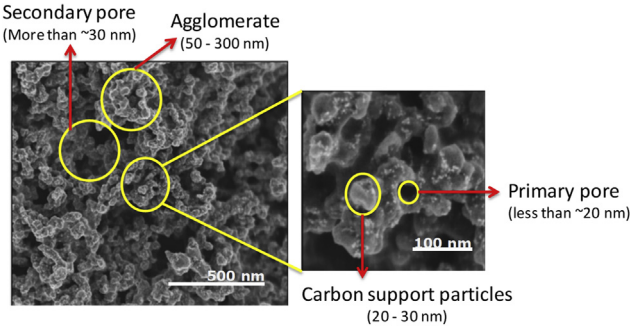

Fig. 1 – SEM image of a catalyst layer showing secondary and primary pores, agglomerates, and carbon support particles.

inside the agglomerates and secondary pores are the void volumes between the agglomerates, which are usually bigger than primary pores. In the present model, the CL microstructure is divided into two scales: i) structure within the agglomerate which consists of carbon particles with Pt particles and ionomer shell around the agglomerate; ii) structure of agglomerates that are connected, with secondary pores between them.

In order to simplify the complex structure of CL, a representative geometry, i.e. unit cell, is developed that has the same microstructural properties as CL. The assumptions that are considered for this CL representative geometry are as follow:

i) Agglomerates are spheres with overlap with simple cubic (SC) arrangement as shown in Fig. 2a, b. It is found that the overlapping spheres are a better representative of agglomerates for CL [4,6,15–17].
ii) Carbon particles have spherical shape and their arrangement is face-centered cubic (FCC) as written on Fig. 2c. However, the arrangement of carbon particles is not playing an important role in deformation model unlike gas diffusivity model [4,6].
iii) Spherical Pt particles are attached to carbon particles on their surface.
iv) Ionomer covers the spherical agglomerates with uniform thickness as shown in Fig. 2c, d.

Fig. 2c shows a schematic of one agglomerate containing carbon particles, Pt particles, and ionomer shell. The overlap of the agglomerates is shown and defined by φ, i.e. the overlap angle. Moreover, ionomer shell around one agglomerate is shown in Fig. 2d, where the holes are the overlap of agglomerates. It should be noted since PSD is an input to the model, unit cell size has a distribution, meaning that a unit cell size is found based on each pore size. Hence, the simplified geometry consists of many unit cell sizes with a distribution similar to PSD. For more details on the calculation of simplified geometry, see Refs. [4,6,18].

The overlapping parameter, ξ, is defined as the ratio of radius of agglomerate to radius of aggregate (i.e. $\xi = r/a$) or as the overlap angle, φ, as it is shown in Fig. 2c. These values are related through Eqs. (1) and (2). The radius of aggregates, or size of unit cell (a), and radius of agglomerates, r, are calculated based on secondary pore sizes (Eq. (8)).

$$\xi = r/a \tag{1}$$

$$\varphi = \cos^{-1}(1/\xi) \tag{2}$$

By considering an FCC arrangement for carbon particles inside the agglomerates, the following equations for agglomerate porosity ($\varepsilon_{agglomerate}$), volume of agglomerates ($V_{agglomerate}$), porosity of catalyst layer (ε_{CL}) and overlapping parameter (ξ) can be written:

$$\varepsilon_{C-Pt} = \varepsilon_C \frac{\rho_{Pt}}{\rho_{Pt} + \rho_C \omega_{Pt/C}} \tag{3}$$

$$\varepsilon_{agglomerate} = \frac{\rho_{Pt}\rho_I \varepsilon_{C-Pt}(1-\varepsilon_{FCC}) + \rho_I(\rho_{Pt} + \rho_C \omega_{Pt/C})\varepsilon_{FCC}}{\rho_I(\rho_{Pt} + \rho_C \omega_{Pt/C}) + \rho_{Pt}\rho_C \omega_{I/C}(1-\varepsilon_{FCC})} \tag{4}$$

$$\varepsilon_{CL} = 1 - \frac{V_{agglomerate}(1-\varepsilon_{agglomerate})}{8a^3} \tag{5}$$

$$V_{agglomerate} = V_{sphere} - 6V_{overlap} = \frac{4}{3}\pi a^3(4.5\xi^2 - 2\xi^3 - 1.5) \tag{6}$$

$$\varepsilon_{CL} = 1 - \frac{\pi(1-\varepsilon_{agglomerate})(4.5\xi^2 - 2\xi^3 - 1.5)}{6} \tag{7}$$

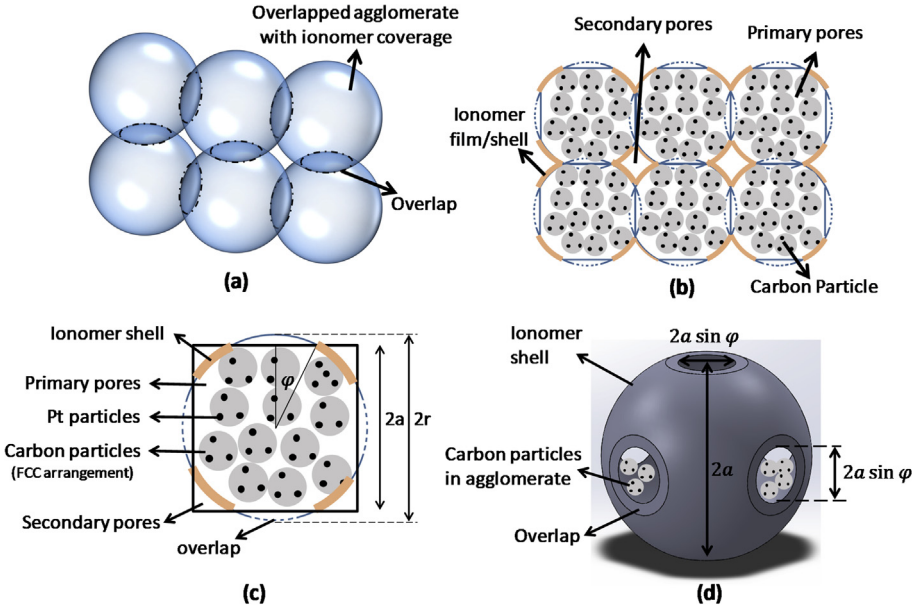

Fig. 2 – Schematic of proposed geometrical model for CL; a) 3D view, b) 2D front view, c) Schematic of one agglomerate showing carbon particles and ionomer shell, d) Geometry of ionomer shell around agglomerates.

$$\xi = \frac{3}{4} + \frac{9}{2\left(4\sqrt{16\Psi^2 - 6\Psi - 45} - 16\Psi + 3\right)^{\frac{1}{3}}} + \frac{1}{4}\left(4\sqrt{16\Psi^2 - 6\Psi - 45} - 16\Psi + 3\right)^{\frac{1}{3}} \quad (8)$$

$$\Psi = \frac{6(1-\varepsilon_{CL})}{\pi\left(1-\varepsilon_{agglomerate}\right)} \quad (9)$$

where, V_{C-Pt} is the total volume of carbon and Pt particles in the agglomerate including the pores inside carbon particle, ε_{C-Pt} is porosity of carbon and Pt particles combined, ρ_I, ρ_{Pt}, and ρ_C are the densities of ionomer, Pt and carbon particles, respectively. $\omega_{I/C}$ and $\omega_{Pt/C}$ are the weight ratio of ionomer to carbon ratio (I/C) and Pt to carbon in CL, respectively. ε_C is the porosity of carbon support particles which is 0.29 as suggested by Voet and Aboytes [19]. ε_{FCC} is the porosity of FCC arrangement which is 0.26 [20]. $\varepsilon_{agglomerate}$ is the porosity of agglomerate, ε_{CL} is the porosity of the proposed unit cell representing CL, Ψ is a dimensionless parameter used to simplify Eq. (8), and V_{sphere} and $V_{overlap}$ are the volume of the sphere and the overlap, respectively.

A method to calculate an equivalent radius from square root of the area (Eq. (11)) was suggested by Bahrami et al. [21], in which one can use the area of the secondary pore (Eq. (10)) shown in Fig. 2a, b. So, an equivalent pore radius for secondary pores can be found as a function of size of unit cell, combining Eqs. (10) and (11). Therefore, the unit cell size (i.e. a) can be found using Eq. (12) for different pore sizes obtained from PSD, which means unit cells in the simplified geometry have different sizes which is dependent on the sizes and volume percentage of pores in CL.

$$r_{pore} = 0.5\sqrt{A_{pore}} \quad (10)$$

$$A_{pore} = 4a^2 - A_{agglomerate} = 4a^2(1 - \tan\varphi) - (\pi - 4\varphi)r^2 \quad (11)$$

$$a = \frac{r_{pore}}{\sqrt{1 - \tan\varphi - \left(\frac{\pi}{4} - \varphi\right)\xi^2}} \quad (12)$$

where, ξ can be found from Eq. (8) and φ can be found using Eq. (2), r_{pore} is the radius of the pore, and A_{sp} is area of the secondary pore. in this model, the ionomer was considered as a spherical shell around agglomerates and its average thickness was found based on the geometry of unit cell and CL ink properties.

$$V_{carbon} = V_{agglomerate}(1 - \varepsilon_{FCC})(1 - \varepsilon_{C-Pt}) \quad (13)$$

$$V_{ionomer} = V_{carbon} * \omega_{I/C} * (\rho_C/\rho_I) \quad (14)$$

$$t_{ionomer} = \frac{V_{ionomer}}{A_{agglomerate}} \quad (15)$$

$$A_{agglomerate} = 4\pi r^2 - 6 \times 2\pi r(r - a) \quad (16)$$

where, $A_{agglomerate}$ is the total area covered by ionomer which is the area around the agglomerate, and $t_{ionomer}$ is the thickness of ionomer covering agglomerate. Using Eqs. (8), (12), and (15), one can build the geometrical model as shown in Fig. 2. Unit cells in the representative geometry have different sizes based on PSD, which introduces a distribution for agglomerate size as well. The agglomerate size distribution obtained from this model is validated with experimental results, see the supplementary data of ref. [4].

Compression of unit cell

After building the geometry of the proposed simplified unit cell, three deformation modes were considered [6]: i) deformation due to Hertzian contact of carbon particles, i.e., compliance; ii) deformation of agglomerates, which can be considered as a packed bed of carbon particles with an FCC arrangement; and iii) deformation of the ionomer shell. After performing a comprehensive study, it was found that the third mode had the dominant deformation in CL. To this end, the compliance of carbon particles and deformation of agglomerates as a packed bed, was neglected. It is also assumed that the carbon particles inside the agglomerates can 'slide' rather freely as rigid particles with negligible friction. Hence, Koiter's model [22] has been used to find the deformation of the proposed ionomer shell that covers the agglomerates, shown in Fig. 2d. Koiter calculated the deformation of a non-shallow hollow spherical shell loaded at vertex, Eqs. (17) and (18).

$$d = \frac{\sqrt{3(1-\nu^2)}}{4}\frac{F\,.\,r}{E_{ionomer}t_{ionomer}^2}\left[1 + \frac{2(1+\nu)}{\pi\lambda^2}\left(\ln\lambda + \gamma_0 - 1 + \frac{\ln 2}{2}\right) + \frac{4}{3\pi\lambda^2}\right] \quad (17)$$

$$\lambda^2 = \sqrt{3(1-\nu^2)}\,\frac{r}{t_{ionomer}} \quad (18)$$

As previously shown in Ref. [6], the CL compression had non-linear behaviour and the reason for such behaviour was the change in microstructure as CL undergoes compression. Therefore, as the porous CL is compressed, porosity decreases, and the material becomes stiffer. This effect has been included in our model by calculating and changing the porosity continuously through out compression.

This procedure can be briefly described as the following: i) the compression is applied in infinite number of steps and after each step, deformation due to a small force increment is found; ii) after each step, a new porosity is calculated based on Eq. (19), which has been widely used in the literature to model different properties of porous media [23–30]; iii) using the new porosity, a new simplified geometry is built; and iv) another force increment is applied and procedure is repeated. Fig. 3 shows a flowchart of the recursive CL compression model developed in this study. The number of steps used in this study is 500, which is large enough for our analytical model.

$$\varepsilon_{new} = 1 - \frac{t_{CL0}}{t_{CL-new}}(1 - \varepsilon_0) \quad or \quad \varepsilon_{new} = 1 - \frac{1}{1 - \frac{\Delta t}{t_{CL0}}}(1 - \varepsilon_0) \quad (19)$$

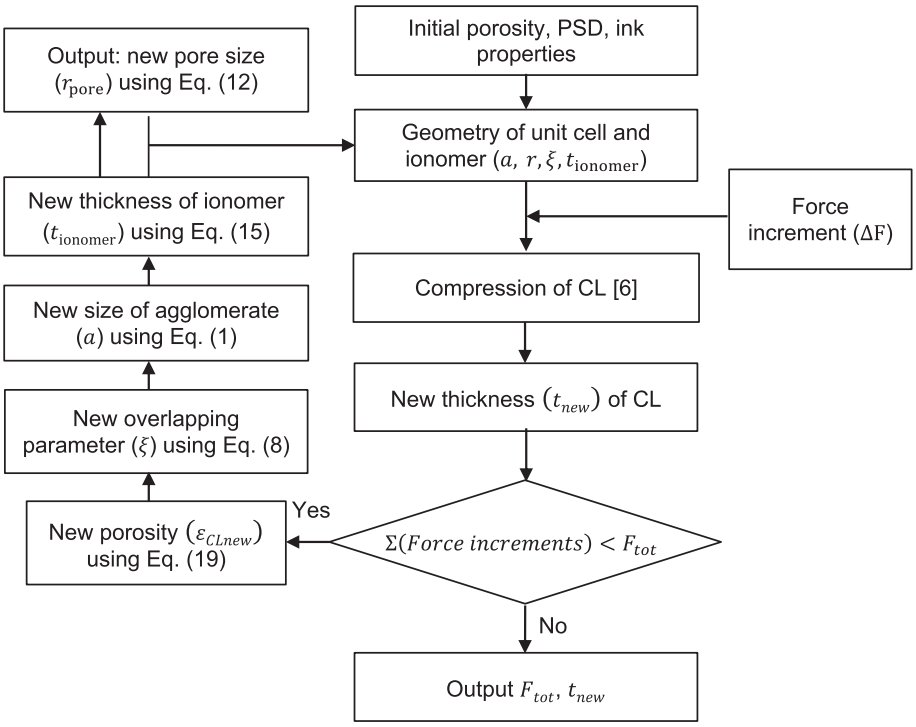

Fig. 3 – Algorithm of the proposed compression model for CL microstructure: recursive model, at each step a new geometry is constructed.

CL microstructure change

Effect of compression on pores

By applying compressive load on CL, shape of the pores is affected. The change occurs on both primary pores and secondary pores, but the change in larger pores is more significant. The reason is that the deformation in larger pores are more and hence their volume reduction is more notable than that of smaller pores. If diameter of both large and small pores decreased by a same percentage, the volume of large pores would decrease more than the volume of small pores because volume is related to the third power of diameter.

Primary pores

The primary pores are between carbon particles inside agglomerates (Fig. 1). And since it is assumed that the particles can slide freely on each other, the primary pores do not change significantly and the change in volume of the primary pores is negligible compared to change of secondary pores. Thus, primary pores are considered to have negligible change with applied pressure on CL. In other words, the size of primary pores and number of them in the CL structure are considered to remain constant during compression. However, because the entire void volume decreases under compression, the volume percentage of primary pores in PSD changes.

Secondary pores

The secondary pores are between the agglomerates and are usually larger than primary pores (Fig. 1), so their change are more significant. As pressure is applied on CL, secondary pores become smaller so their contribution in total void volume changes as well. As described in the modeling part of this study (section Compression of unit cell), the proposed unit cell is created at each step of the recursive function by considering the change in the porosity, and accordingly the microstructure. Thus, one can find how the geometry of pores are changing under compression. By knowing the deformation of CL after a force increment, strain can be found as well as the new porosity. Having the new porosity, a new geometry can be built and based on that, new pore sizes from each unit cell size can be calculated.

Effect of compression on pore size distribution

Based on the proposed model for deformation of CL under compressive load, one can find the change of each secondary pore and finally the change in PSD. Using the inputs of the geometrical model (PSD, porosity, and ink properties), the proposed simplified geometry of CL, i.e. the parameters a, r, ξ, and t_{ionomer}, can be found from Eqs. (1)–(15). Once the geometry is known, the deformation and strain of CL under a force increment can be calculated from Eq. (17). Using Eq. (19), a new porosity after a force increment can be found, and a new overlapping parameter, ξ, can be obtained from Eq. (8). The geometry of the simplified CL in the model can then be recalculated since the overlapping parameter is changed. Using Eq. (1), one can find the new size of the unit cell (a) and accordingly, a new pore radius can be obtained from Eq. (12). This procedure should be repeated for all the pore sizes to find the change of diameter of secondary pores. As shown in the flowchart of the proposed model (Fig. 3), new geometrical

parameters (r_{pore}, a, and $t_{ionomer}$) can be obtained after a force increment and are used to form a new geometry. This cycle should be repeated until the desired force is reached. Using the model, the change of each secondary pore diameter with compressive load is obtained.

Knowing the change of each pore size under compression, PSD at any given compressive load can be calculated. It is also assumed that during compression of CL, the number of pores remains constant and their size changes.

Results and discussions

Effect of compression on pore size

The input parameters of the model are pore size distribution, porosity, thickness, ink properties, and compressive load. The properties of CL samples used for this study are listed in Table 1. The initial PSD of each sample was measured using N_2 adsorption porosimetry (Autosorb iQ-MP, Quantachrome Instruments) and the initial porosity of the catalyst layers were measured using a custom-made densitometer at Automotive Fuel Cell Corporation (AFCC). The initial thickness of each sample was also measured using different techniques which were explained in our previous paper [5]. Another important sample preparation step of CL that has a considerable effect on microstructure of CL is dry milling time, which is not a direct input to the model; however, the effect of dry milling time is reflected in PSD of each sample. Also, the ionomer to carbon weight ratio (I/C ratio) of CL samples was determined by the weight of ionomer (gr) to weight of carbon (gr) that was used to prepare the ink.

As described before, the proposed model reconstructs the simplified geometry at each step of compression (section Effect of compression on pore size distribution), which means that the change of pore sizes can be found at any given pressure. In this paper, the maximum applied pressure is 5 MPa which is more than the typical compressive load that exists in PEM fuel cells. This pressure is considered since it aligns with our previous work in which deformation of CL was measured and modeled up to 5 MPa [5,6]. Fig. 4 shows the change of secondary pore size as function of compression for CL Design 2; the following can be concluded from the figure:

i) The change of pore size as a function of compression is almost linear for all the pore sizes. Only three pore sizes (273 nm, 91 nm, and 50 nm) are shown here since other pores followed the same trend.

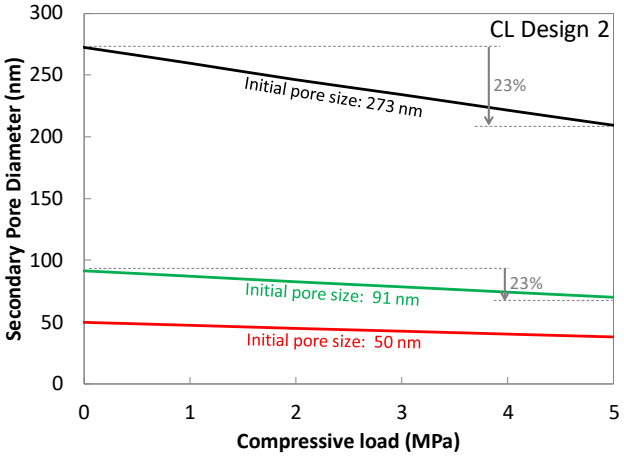

Fig. 4 – Secondary pore size as function of compressive load for CL Design 2, the size of each pore is reduced by the same percentage since the Koiter model [22] is used to find deformation of CL.

ii) The change in larger pores is more significant since their deformation is larger. However, the percentage decrease for all the pores are found to be the same (23%) because the Koiter model, Eq. (17), used for deformation of CL is linear.
iii) The volume change of the bigger pores is more significant than smaller pores since volume is proportional to third power of pore size.
iv) The volume change of primary pores is negligible, so it is neglected in this study.

It should be mentioned that the results shown in Fig. 4 is only for CL Design 2 and clearly the percentage change of pore sizes will be different for various CL Designs. The reason for this difference is the difference in microstructure (i.e. porosity, PSD, I/C ratio) of each Design which are the input parameters to the model. Also, the strain of each sample is not the same which is also why the change in pore sizes for various CL Designs are different.

Similar trend is seen for other CL Designs. Fig. 5 shows the change of pore sizes as function of compressive load for the other three CL Designs used in this study. Not all the secondary pore sizes are shown because the rest of them had the same percentage decrease. As shown in Fig. 5, various Designs has different percentage change in their pore sizes. However, this percentage change is the same for different pore sizes in each of the Designs. The results show that the secondary

Table 1 – Properties of different CLs used in this study (model inputs), design numbers are the same as our previous work [5].

CL Design number	I/C ratio (gr/gr)	Densitometer porosity (%)	Thickness (μm)	Mechanical properties of ionomer (measured)
Design 2	0.9	52.0	6.9	$E_{ionomer} = 93$ MPa$\nu = 0.3$
Design 3	0.7	52.4	6.1	
Design 4	0.7	50.5	4.6	
Design 5	0.9	33.4	6.3	

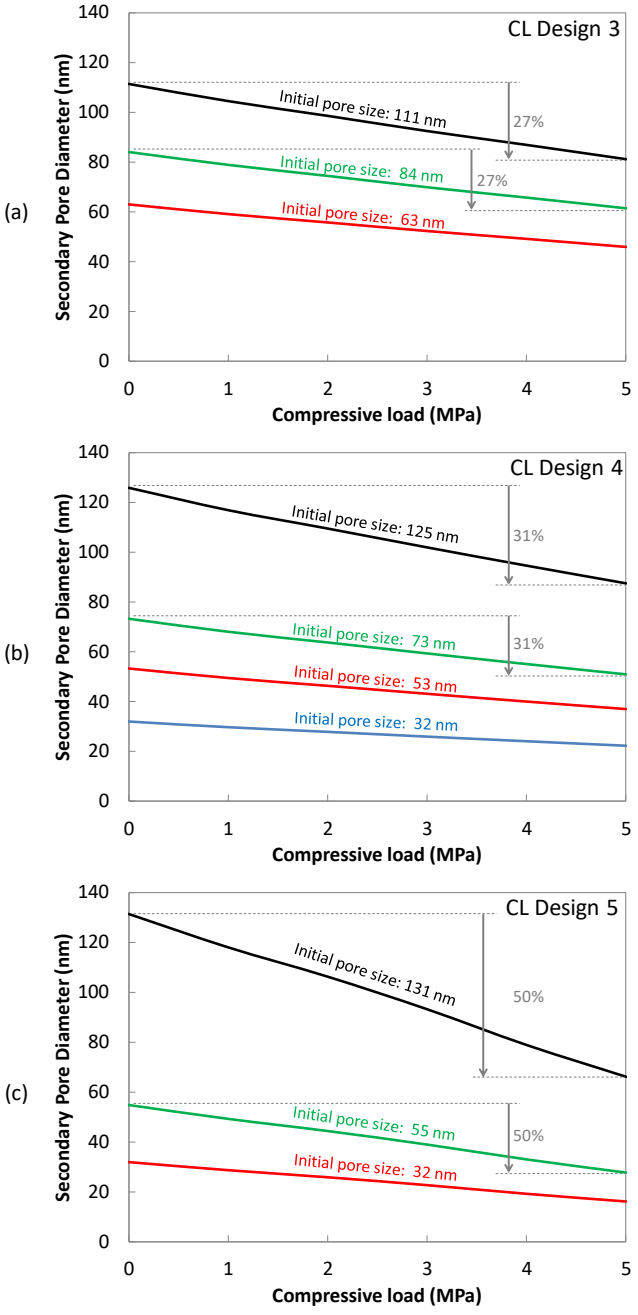

Fig. 5 – Secondary pore diameter as function of compressive load for: (a) CL Design 3, (b) CL Design 4, and (c) CL Design 5; the size of each pore is reduced by the same percentage.

pores become smaller by 20–50%, depending on its initial microstructure, which is significant and should be considered in modelling transport properties of CL under compression.

Effect of compression on pore size distribution

Having the change of pore sizes as a function of compressive load on CL, one can find the PSD after the pressure is applied assuming that the number of pores remains the same. Fig. 6 shows the effect of 2 and 5 MPa compressive load on the

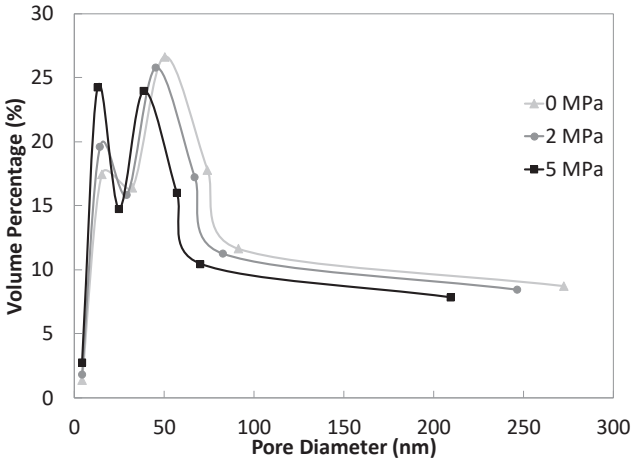

Fig. 6 – Pore size distribution of CL Design 2 under compression up to 5 MPa (obtained from model).

PSD of CL Design 2. Not to clutter Fig. 6, only the PSD after 2 MPa and 5 MPa are shown. PSD at 0 MPa is the measurement results using N_2 adsorption porosimetry. It should be mentioned that the points are connected with a line for better visualization of PSD change with compression. The following can be concluded from Fig. 6:

i) Diameter of pores decreases with compression and the PSD shifts to the left, which means that the pores become smaller.
ii) The change in larger secondary pores are more notable than smaller secondary pores.
iii) The volume percentage of the larger pores decreases, and volume percentage of smaller pores increases (~20 nm pore shown in Fig. 6). This does not mean that the number of smaller pores or their size increases. This can be explained since by increasing compressive load, larger pores deform more so their volume decreases more. Since the total void volume decreases significantly, the volume percentage of small pores increases. To this end, a jump in the percentage of smaller pores can be seen in Fig. 6.

Similar trend is seen for the other three CL Designs and secondary pores become smaller as shown in section Effect of compression on pore size. Figs. 7–9 show PSD under compression for CL Designs 3, 4, and 5, respectively. The lines are drawn for better visualization of the trend. In Fig. 7, a shift toward smaller pores can be seen, which is caused by the reduction in pore sizes. Also, an increase in volume percentage of smaller pores is visible, which is because of the decrease in total void volume of CL. As compressive load increases, volume percentage of larger pores (larger than ~20 nm) decreases but volume percentage of smaller pores (less than ~20 nm) increases, which causes the peak to move to the left. Moreover, PSD change for CL Design 4 (Fig. 8) shows that smaller pores have more volume percentage in PSD under 5 MPa pressure, which again is the result of decrease in the size of the larger pores. Similarly, PSD for CL Design 5 (Fig. 9) shifts toward the left which means that larger pores decreases

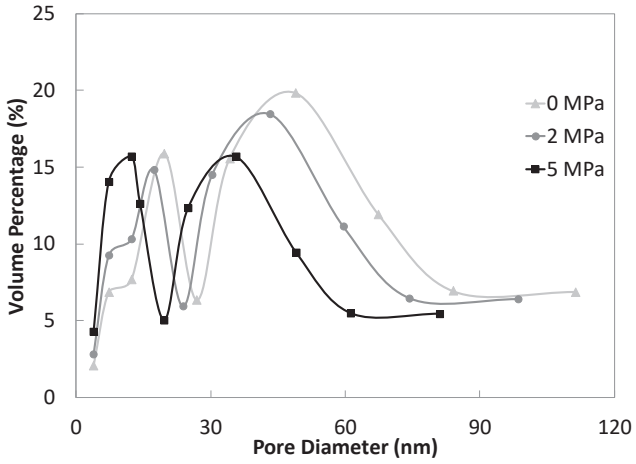

Fig. 7 – Pore size distribution of CL Design 3 under compression up to 5 MPa.

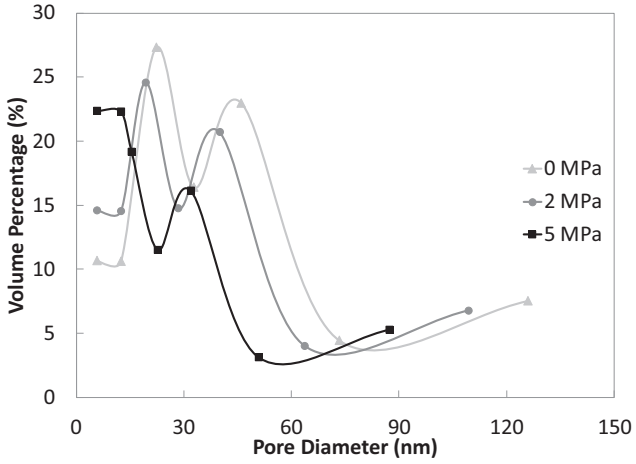

Fig. 8 – Pore size distribution of CL Design 4 under compression up to 5 MPa.

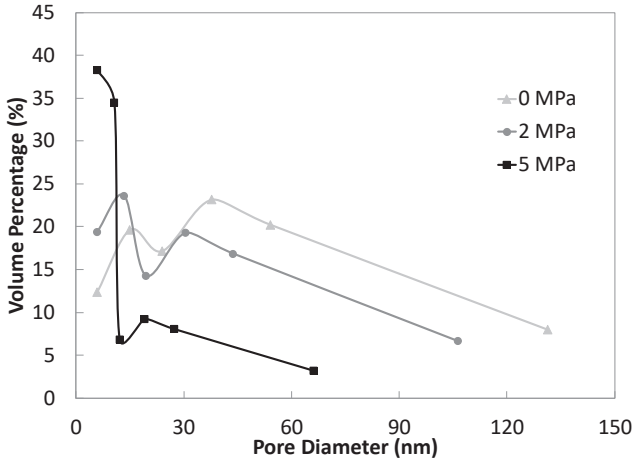

Fig. 9 – Pore size distribution of CL Design 5 under compression up to 5 MPa.

in size, and the volume percentage of smaller pores increases. PSD change of CL Design 5 under compression is the most among the four samples because the reduction in pore size for this Design is 50% (Fig. 5c) which is about twice the other Designs. Hence, a significant jump in volume percentage of smaller pores can be seen in Fig. 9 for CL Design 5.

The change in PSD under compression that are obtained by our model in this study is similar to another study which is performed by Kosowska et al. [31] on a different polymer porous material for tissue engineering. They measured PSD of a polymer-based porous materials after drying the samples under different compressive loads. They investigated the influence of foaming process parameters such as pressure, duration, and temperature and found out that applying more compressive load caused the pores to be smaller. They reported that by applying compression, the volume percentage of smaller pores increased, and volume percentage of larger pores decreased. The results of the present study showed the same trend even though the material and its applications are different.

Effect of compression on porosity

The change in PSD alone may not be the best representative of microstructure change of CL under compression. Along with PSD, porosity should also be considered for better understanding of this porous layer. Fig. 10 shows the porosity change of each Design, which is obtained from the model and validated with experimental results from our previous papers [5]. As shown in Fig. 10, porosity of each Design is decreased under compression; the percentage decrease of the porosities for each Design is different (11–17%) since the porosity reduction is related to strain of CL at any given pressure. A better understanding of transport properties of CL can be obtained by having both PSD and porosity under compression. Although the pressure range for PEM fuel cell is not as high as 5 MPa, this study shows the trend for microstructure change of CL under compressive load.

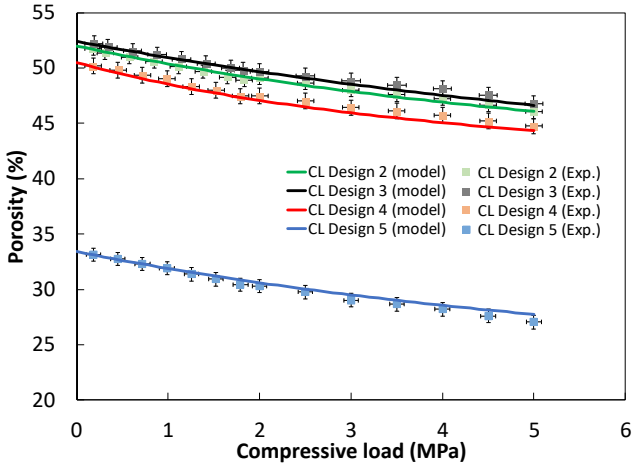

Fig. 10 – Porosity of CL Designs under compression up to 5 MPa (obtained by model and validated using experimental results [5]).

The core of the presented model, changing the simplified geometry at each step, can be extended to any other porous layer. This method is used for other porous layers as well to find deformation under compression, such as Gas Diffusion Layer [32] and Aerogel Blankets [30].

Conclusions

In this study, pore size distribution under compression was studied using our developed model. This model used a representative geometry to simplify the random porous structure of CL. The input parameters of the model were pore size distribution, porosity, thickness, ink properties, and compression. Pore sizes, PSD, and porosity of four different CL samples with different properties were found under compressive load up to 5 MPa. PSD and porosity, as representatives of CL microstructure, found to change significantly under compression. The model showed that depending on the CL sample, pore diameter decreased between 20 and 50% under 5 MPa pressure, a significant change that should be considered in modeling transport properties. Moreover, PSD of each sample was found under compression. The results indicated that the volume percentages of smaller pores increased because of a significant decrease in volume of the larger pores. Also, porosity of the CL samples under compression was modeled and compared with experimental results during compression, which showed a decrease of 11–17% depending on initial CL microstructure.

Acknowledgements

This research was supported by funding from the Natural Sciences and Engineering Research Council of Canada (NSERC) Collaborative Research and Development (Grant No. CRDPJ 452170-13) and Automotive Fuel Cell Corporation (AFCC). AFCC Structure, Properties & Performance Research Division is also acknowledged for their technical support.

REFERENCES

[1] Tang Y, Santare MH, Karlsson AM, Cleghorn S, Johnson WB. Stresses in proton exchange membranes due to hygro-thermal loading. J Fuel Cell Sci Technol 2006;3:119. https://doi.org/10.1115/1.2173666.

[2] Kai Y, Kitayama Y, Omiya M, Uchiyama T, Kato M. Crack formation on membrane electrode assembly (MEA) under static and cyclic loadings. J Fuel Cell Sci Technol 2012;10:143. https://doi.org/10.1115/FuelCell2012-91164.

[3] Kusoglu A, Karlsson AM, Santare MH, Cleghorn S, Johnson WB. Mechanical response of fuel cell membranes subjected to a hygro-thermal cycle. J Power Sources 2006;161:987–96. https://doi.org/10.1016/j.jpowsour.2006.05.020.

[4] Salari S, Stumper J, Bahrami M. Direct measurement and modeling relative gas diffusivity of PEMFC catalyst layers: the effect of ionomer to carbon ratio, operating temperature, porosity, and pore size distribution. Int J Hydrogen Energy 2018;43:16704–18. https://doi.org/10.1016/j.ijhydene.2018.07.035.

[5] Malekian A, Salari S, Tam M, Oldknow K, Djilali N, Bahrami M. Compressive behaviour of thin catalyst layers. Part I - experimental study. Int J Hydrogen Energy 2019;44:18450–60. https://doi.org/10.1016/J.IJHYDENE.2019.04.134.

[6] Malekian A, Salari S, Tam M, Djilali N, Bahrami M. Compressive behaviour of thin catalyst layers. Part II - model development and validation. Int J Hydrogen Energy 2019;44:18461–71. https://doi.org/10.1016/J.IJHYDENE.2019.04.135.

[7] Uchiyama T, Kato M, Ikogi Y, Yoshida T. Mechanical degradation mechanism of membrane electrode assemblies in buckling test under humidity cycles. J Fuel Cell Sci Technol 2012;9:061005. https://doi.org/10.1115/1.4007814.

[8] Uchiyama T, Kumei H, Yoshida T. Catalyst layer cracks by buckling deformation of membrane electrode assemblies under humidity cycles and mitigation methods. J Power Sources 2013;238:403–12. https://doi.org/10.1016/j.jpowsour.2013.04.026.

[9] Kai Y, Kitayama Y, Omiya M, Uchiyama T, Kumei H. In situ observation of deformation behavior of membrane electrode assembly under humidity cycles. J Fuel Cell Sci Technol 2014;11:051006. https://doi.org/10.1115/1.4028155.

[10] Sassin MB, Garsany Y, Gould BD, Swider-Lyons K. Impact of compressive stress on MEA pore structure and its consequence on PEMFC performance. J Electrochem Soc 2016;163:F808–15. https://doi.org/10.1149/2.0291608jes.

[11] Shen Y. Mechanical degradation of membrane Electrode assemblies in proton exchange membrane fuel cells. University of Waterloo; 2017.

[12] Ogawa S, Babu SK, Chung HT, Zelenay P, Padgett E, Muller DA, Kongkanand A, Litster S. Microstructural modeling of PEFC catalyst layer performance and durability. In: Meet. Abstr. The Electrochemical Society; 2017. p. 1374.

[13] Zenyuk IV, Kumbur EC, Litster S. Deterministic contact mechanics model applied to electrode interfaces in polymer electrolyte fuel cells and interfacial water accumulation. J Power Sources 2013;241:379–87. https://doi.org/10.1016/j.jpowsour.2013.03.165.

[14] Ahadi M, Tam M, Saha MS, Stumper J, Bahrami M. Thermal conductivity of catalyst layer of polymer electrolyte membrane fuel cells: Part 1 – experimental study. J Power Sources 2017;354:207–14. https://doi.org/10.1016/j.jpowsour.2017.02.016.

[15] Ahadi M, Putz A, Stumper J, Bahrami M. Thermal conductivity of catalyst layer of polymer electrolyte membrane fuel cells: Part 2 – analytical modeling. J Power Sources 2017;354:215–28. https://doi.org/10.1016/j.jpowsour.2017.03.100.

[16] Salari S, McCague C, Tam M, Stumper J, Bahrami M. Modeling diffusivity in catalyst layer of a PEMFC based on a unit cell approach. In: 228th ECS Meet.; 2015. p. 50. Phoenix.

[17] Salari S, Stumper J, Bahrami M. Through plane gas diffusion of catalyst layer of PEMFC: bimodal unit cell modeling. In: 27th Inernational Symp. Transp. Phenom. Honolulu; 2016.

[18] Malekian A. Compressive behaviour of thin porous layers with application to PEM fuel cells. Simon Fraser University; 2019. https://theses.lib.sfu.ca/5185/show.

[19] Voet A, Aboytes P. Porosity of carbon blacks. Carbon N Y 1971;9:135–8. https://doi.org/10.1016/0008-6223(71)90126-6.

[20] Ellis AB. Teaching general chemistry: a materials science companion. Am Chem Soc 1993. https://books.google.ca/books?id=igXwAAAAMAAJ.

[21] Bahrami M, Yovanovich MM, Culham JR. Pressure drop of fully-developed, Laminar flow in microchannels of arbitrary cross-section. J Fluids Eng 2006;128:1036–44. https://doi.org/10.1115/1.2234786.

[22] Koiter WT. A spherical shell under point loads at its poles. Brown Univ Providence RI DIV of Applied Mathematics; 1962.

[23] Zhou Y, Jiao K, Du Q, Yin Y, Li X. Gas diffusion layer deformation and its effect on the transport characteristics and performance of proton exchange membrane fuel cell. Int J Hydrogen Energy 2013;38:12891–903. https://doi.org/10.1016/j.ijhydene.2013.05.150.

[24] Flückiger R, Freunberger SA, Kramer D, Wokaun A, Scherer GG, Büchi FN. Anisotropic, effective diffusivity of porous gas diffusion layer materials for PEFC. Electrochim Acta 2008;54:551–9. https://doi.org/10.1016/j.electacta.2008.07.034.

[25] Gigos PA, Faydi Y, Meyer Y. Mechanical characterization and analytical modeling of gas diffusion layers under cyclic compression. Int J Hydrogen Energy 2015;40:5958–65. https://doi.org/10.1016/j.ijhydene.2015.02.136.

[26] Xu G, LaManna JM, Clement JT, Mench MM. Direct measurement of through-plane thermal conductivity of partially saturated fuel cell diffusion media. J Power Sources 2014;256:212–9. https://doi.org/10.1016/j.jpowsour.2014.01.015.

[27] Jiao K, Park J, Li X. Experimental investigations on liquid water removal from the gas diffusion layer by reactant flow in a PEM fuel cell. Appl Energy 2010;87:2770–7. https://doi.org/10.1016/j.apenergy.2009.04.041.

[28] Feser JP, Prasad AK, Advani SG. Experimental characterization of in-plane permeability of gas diffusion layers. J Power Sources 2006;162:1226–31. https://doi.org/10.1016/j.jpowsour.2006.07.058.

[29] Khajeh-Hosseini-Dalasm N, Sasabe T, Tokumasu T, Pasaogullari U. Effects of polytetrafluoroethylene treatment and compression on gas diffusion layer microstructure using high-resolution X-ray computed tomography. J Power Sources 2014;266:213–21. https://doi.org/10.1016/J.JPOWSOUR.2014.05.004.

[30] Hoseini A, Malekian A, Bahrami M. Deformation and thermal resistance study of aerogel blanket insulation material under uniaxial compression. Energy Build 2016;130:228–37. https://doi.org/10.1016/j.enbuild.2016.08.053.

[31] Kosowska K, Henczka M. The influence of supercritical foaming conditions on properties of polymer scaffolds for tissue engineering. Chem Process Eng – Inz Chem i Proces 2017;38:535–41. https://doi.org/10.1515/cpe-2017-0042.

[32] Malekian A, McCague C, Salari S, Djilali N, Bahrami M. Compression of pem fuel cell gas diffusion layers: analytical model and experimental validation. In: 27th Int. Symp. Transp. Phenom., Honolulu; 2016.